CHAPTER V

HIGH TEMPERATURE SUPERCONDUCTOR/SEMICONDUCTOR HYBRID MICROWAVE DEVICES AND CIRCUITS

Robert. R. Romanofsky and Félix A. Miranda

National Aeronautics and Space Administration

Glenn Research Center, Cleveland, Ohio 44135

example, ten times as much energy is required to attain 9.5 K than 77 K operation. The technology for compact and reliable integrated cryo-electronics near 77 K is in hand.

Progress in the deposition of HTS thin films on low loss microwave substrates such as Lanthanum Aluminate ($LaAlO_3$), Magnesium Oxide (MgO), and Sapphire (Al_2O_3), amongst others, has resulted in thin films with microwave surface resistance (R_s) values orders of magnitude lower than those of conventional conductors such as gold (Au) and copper (Cu) [7-9]. These developments have led to demonstrations of superconducting passive microwave circuits such as resonators and filters [10,11]. In the semiconductor arena interesting results at cryogenic temperatures have been observed in the last decade. For example, useful changes have been observed in the carrier mobility and sheet resistance of semiconducting materials when the temperature is lowered from room temperature to 100 K or below, depending on the material and the doping level. This is particularly true for the case of GaAs-based devices [12]. The combination of passive HTS-based microwave components with active semiconductor devices and circuits for integration into microwave subsystems can offer additional advantages such as reduced loss and noise [13]. It has also been demonstrated that HTS and ferroelectric thin film technology could be used to fabricate tunable HTS/ferroelectric microwave components [14-18]. Therefore, in this review we will discuss the design, fabrication, and performance of various superconducting hybrid microwave devices and circuits, and the unique challenges of cryogenic microwave engineering. It is worth mentioning that the experimental results discussed here very often represent proof-of-concept (POC) devices and circuits. In view of the continuous optimization of the material properties of HTS, semiconductor, and ferroelectric thin films, and the advances in processing techniques, the results presented here will surely undergo modifications as the field matures.

V.2.2.1 Laser Ablation

A technique that has proven to be very effective for the deposition of HTS thin films is pulsed laser deposition (PLD) [19-20]. In this technique laser pulses (KrF, ArF excimer lasers, or a Nd-YAG laser are among the most commonly used) are fired onto a stoichiometric target of the HTS material to be deposited (e.g., YBCO). This results in a plasma "plume" of ejected material from the target which condenses onto a substrate mounted on a heated holder and kept at temperatures near 800°C. A schematic of this configuration is shown in figure 1. The main advantage of this technique is that the laser produced plume is stoichiometric in composition, and therefore the resulting films are also stoichiometric in composition. Since the films are grown in an oxygen atmosphere (e.g., 100 mtorr), the superconducting phase is attained in-situ during the laser ablation process eliminating the need of a post-deposition or "ex-situ" annealing treatment. Thus, the major advantages of this technique are that a stiochiometric target can be used as the source material, a higher deposition rate of the HTS material relative to off-axis magnetron sputtering, and easy optimization of the film composition and crystallinity by the adjustment of the main deposition parameters. These are the energy density of the laser pulses, the distance between the target and substrate, and the deposition temperature. Because of these attributes laser ablation has become the technique of choice in the fabrication of high quality HTS films.

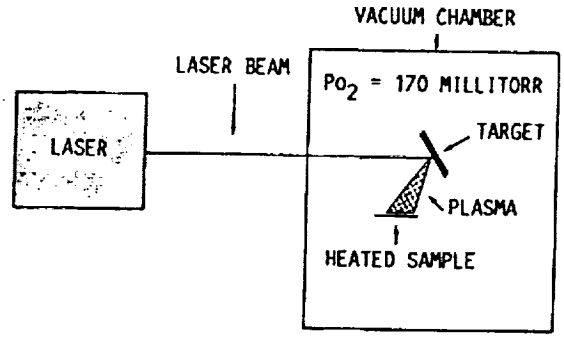

Figure 1. - Schematic of laser ablation experiment.

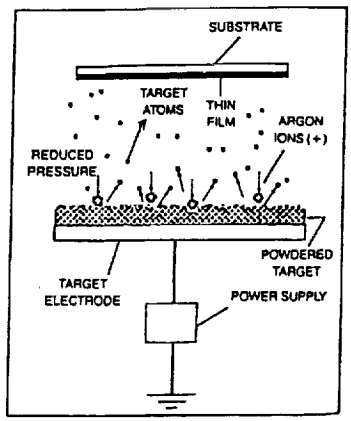

Figure 2. Schematic representation of the rf magnetron sputtering deposition system.

V.2.2.3. Sequential Evaporation

The deposition of YBCO superconducting thin films using sequential evaporation was first reported by B.Y. Tsaur, et al. [25]. In this technique, the multilayer film is made by electron beam evaporation of alternate layers of either Cu, Ba, and Y, or Cu, BaF_2, and Y. The basic three-layer stack is repeated to give a total of 12 to 18 layers. This technique allows for the deposition of films with little spatial variation of stoichiometry across the substrate as all components of the film are evaporated form the same point in space. The stoichiometry of the films is easily adjusted by controlling the thickness of the individually deposited layers. However, this deposition technique requires post-deposition annealing of the film in order to attain the superconducting phase. This annealing can last 0.5 hr at 850°C. During the annealing the sample is exposed to ultra high purity oxygen which has been bubbled, at room temperature, through water. The water vapor hydrolizes the BaF_2 to form BaO and HF. Dry oxygen is then used for the remainder of the annealing process. The temperature is then ramped to 450°C at a rate of -2°C per minute. The samples are held at this temperature for 6 hr and then the temperature is ramped to room temperature also at a rate of 2°C per minute.

oxygen is leaked into the system through a nozzle near the substrate holder. The chamber pressure in the system during the deposition process is maintained at around $5x10^{-5}$ torr. Evaporation rates of the components during the process range from 0.8 to 3.2 Å per second. Finally, the as deposited film are annealed in a furnace following a two-step

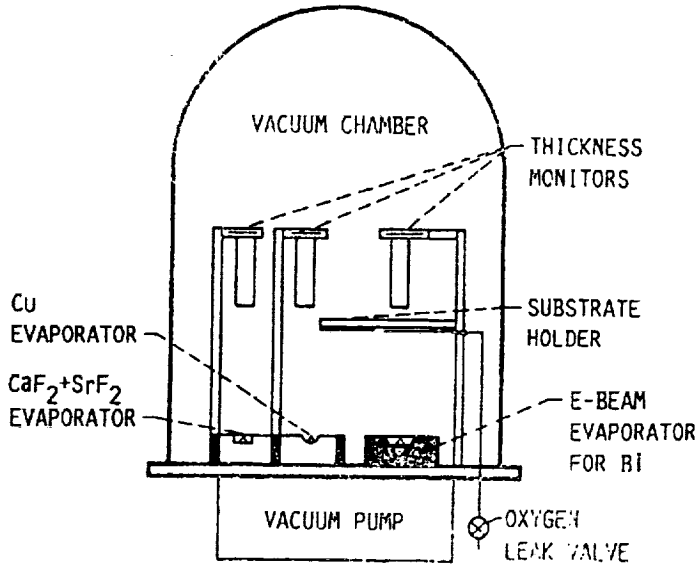

Figure 3. Co-evaporation set up for Bi, CaF_2 + SrF_2 and Cu.

procedure. The fist step of the annealing is performed at 750°C in wet oxygen for about 30 to 60 minutes. This step was performed to decompose the fluorides so that the fluorine will react with the H_2O molecules forming volatile hydrogen fluoride gas (HF). The second annealing step is performed to form the superconducting phase. This step is performed at 850°C for about 5 to 15 minutes. Afterwards, the sample is allowed to cool down slowly (~2°C per minute) to room temperature before removing it from the deposition system.

V.2.3 Microwave Substrates

The special problems as well as the merits associated with constructing microwave circuits at cryogenic temperatures have been studied for many years. For example, it is desirable to minimize physical circuit size which necessitates high dielectric constant

constant of 22-24 at room temperature, changing less than 10% when cooled to cryogenic temperatures [41]. It also has loss tangents of 10^{-4} and 10^{-5} at room temperature and 77 K, respectively, and an excellent lattice match with the high-T_c superconductors [42]. These properties make $LaAlO_3$ very suitable for operation at microwave frequencies. However, this susbtrate is characterized by twining structures that should be taken into consideration during circuit fabrication.

The properties of the $LaGaO_3$ substrates are very similar to those of $LaAlO_3$. It has a dielectric constant of 25 at room temperature and a good lattice match with the high-T_c superconductors [40]. Table I summarizes some of the most relevant properties of the most commonly used substrates for HTS thin film deposition.

TABLE I: Microwave Substrates for HTS Thin Films

Material	Structure (298 K)	Dielectric Constant	Loss Tangent (298 K)	Lattice Size (Å)	Lattice Mismatch	Remarks
MgO	cubic	9.8	$3.0x10^{-4}$	4.178	a=11.0% c=12.8%	Small area, good for "in-situ" film growth, reacts with O_2
$LaAlO_3$	psudo-cubic	22-24	$5.8x10^{-4}$	3.792	a=0.7% c=2.6%	Large area, twinning, very high quality films
$LaGaO_3$	Ortho-rhombic	25	$1.8x10^{-3}$	3.902	a=2.1% c=0.2%	Large area, phase transitions at 140 and 400°C may cause surface roughness (steps)
$SrTiO_3$	cubic	~300 @ 300 K ~1900@ 80 K	~0.03@300 K ~0.06@ 80 K	3.905	a=2.2% c=0.3%	Small area, high quality films

determine the reflection and transmission coefficients. A typical implementation of this technique taken from [48] is shown in figure 4.

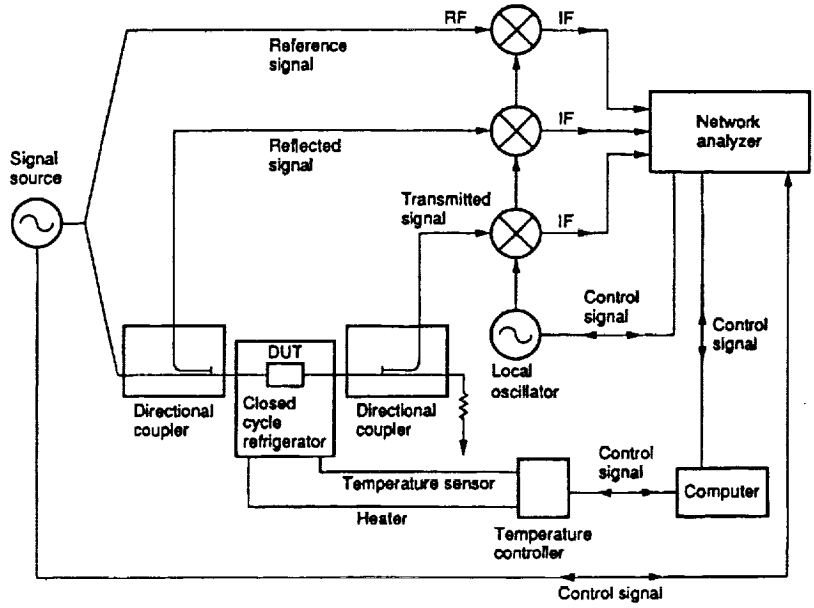

Figure 4. Apparatus for measuring microwave transmitted power through HTS thin films

V.2.4.2. Complex Conductivity

The complex conductivity of a HTS thin film can be determined by measuring the transmission of a microwave signal through a superconducting thin film. For a film of thickness d deposited onto a substrate of thickness t and refractive index n, that covers the entire cross section of a rectangular waveguide propagating the TE_{01} mode (see Figure 5), the fractional transmitted power coefficient **T** and the phase shift φ may be written as,

$$\mathbf{T} = 4n^2\{n^2\cos(k_0nt)[(k_0dR)^2+(2+k_0dI)^2]+\sin^2(k_0nt)[(k_0dR)^2+(n^2+1+k_0dI)^2]+...$$

$$...+(2nk_0dR)\sin(k_0nt)\cos(k_0nt)(n^2-1)\}^{-1} \qquad (V.1)$$

$$\varphi = \arctan\{\cos(k_0t)[(nk_0dR)\cos(k_0nt)+(n^2+1+k_0dI)\sin(k_0nt)]-$$

$$\sin(k_0t)[n(2+k_0dI)\cos(k_0nt)-...$$

the metallic character of these films is evidenced by the positive slope of **T**. Note that at the onset of superconductivity, the transmitted power decreases abruptly leveling off at low temperatures. Also, in the normal state the measured relative phase shift $\Delta\varphi = \varphi_{300\,K} - \varphi(T)$ is nominally constant, while below the onset of the transition one can observe that an abrupt change in takes place. These two parameters are then used to obtain σ^* for the superconducting film by using eqs. (V.1)-(V.4). Figure 7 shows the real (σ_1) and imaginary (σ_2) parts of σ^* as a function of temperature for a YBCO thin film on $LaAlO_3$. In the normal state (i.e., $T>T_c$), σ_1 exhibits a metallic behavior as a function of temperature whereas σ_2 remains very close to zero as expected for a good conductor, which is the typical behavior expected for a superconductor above T_c . Both σ_1 and σ_2 increase rapidly when the film is cooled through the transition temperature. The behavior below T_c is quite different for the two parameters with σ_1 reaching a maximum followed up by a rapid decrease at temperatures not far below the transition temperature, while σ_2 exhibits a monotonic increase with decreasing temperature.

and $1/T_1$ decrease exponentially to zero as the quasiparticles above the gap are frozen out [50]. However, it has been shown that $1/T_1$ for quasiparticles of the chain forming Cu(1) and planar Cu(2) lattice sites decreases rapidly when the films cools through T_c

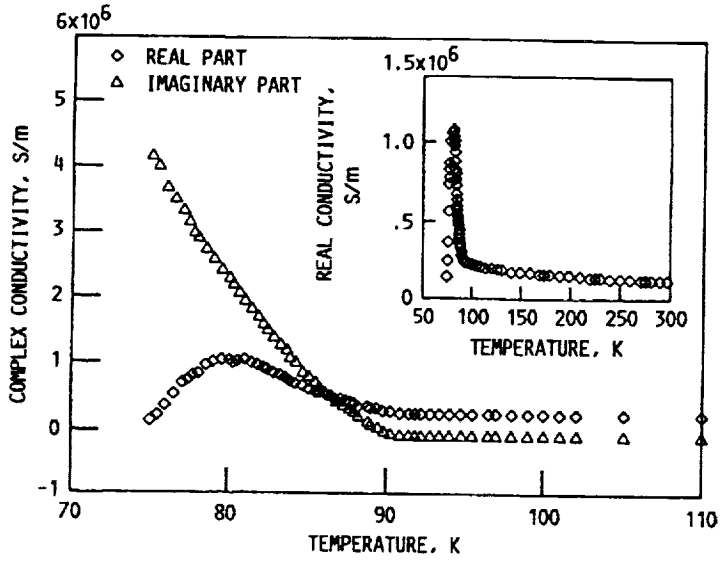

Figure 7. Real and imaginary parts of the microwave conductivity versus temperature at 30.6 GHz for a laser-ablated $YBa_2Cu_3O_{7-\delta}$ thin film (490 nm) on $LaAlO_3$.

[51]. If the observed behavior of σ_1 is indeed due to intrinsic properties of the superconducting state then this type of response may be due to a non-isotropic energy gap or to a superconductor whose behavior deviates from that predicted by the BCS theory. The latter seems to be the most probable scenario and even today there are strong efforts being made in developing suitable models for the superconducting mechanism in the HTS compounds.

the microstripline resonator technique. This technique capitalizes in the relationship between the resonant frequency and the penetration depth as shown by the following expression:

$$v_{ph}=1/(LC)^{0.5}=[c/(\varepsilon_{eff})^{0.5}][1+(\lambda/h)\coth(t/\lambda)+(wR_n/2\pi h^2\omega\mu_o)\coth(t'/\delta)(1-(w'/4h)^2)]^{-0.5} \quad (V.7)$$

where t and t' are the thickness of the HTS microstrip and the normal conductor ground plane, respectively, w is the microstrip width, w' is the conductor width corrected for thickness (i.e., the effective electrical microstrip width), $R_n=(\mu_o\rho\omega/2)^{0.5}$ is the surface resistance of the normal conductor ground plane, δ is the normal conductor skin depth, and $\omega=2\pi f$, where f is the frequency. For ring resonators that satisfy $w/h<1$ and where its mean circumference ($l=2\pi R$) >>w, we have at resonance,

$$l=n\lambda_g=nv_{ph}/f \quad (V.8)$$

where n is the order of the resonance. The kinetic inductance ($L_k(T)$), associated with the inertial mass of the charge carriers, is strongly dependent on the penetration depth. Hence, the shift in resonant frequency with temperature can, in principle, yield a sensitive measure of $\lambda(T)$. However, extracting the zero temperature penetration depth $\lambda(0)$ generally requires the assumption of a particular theoretical model to which the data are curve fit. The situation is exasperated by the complex interdependency among variables such as film thickness (t), circuit geometry including strip width (w) and substrate thickness (h), critical temperature (T_c), and $\lambda(0)$. The penetration depth is also sensitive to the quality of the film, especially near its surface, as well as the transition width (ΔT), which is an indicator of phase purity. Some studies have focused only on extremely low impedance lines [53] or strictly low temperature (i.e. $T<Tc/2$) $\lambda(T)$ dependence [54]. For most practical microwave applications, line impedances will be in the neighborhood of 50 Ω, and film thickness will be of the same order as the penetration depth. Experimental investigations using strip transmission lines near T_c have invariably revealed a strong deviation from theory [55-57] when $t\sim\lambda$. The disagreement can be attributed, at least in part, to the susceptance coupled into the resonator from the gap discontinuity as well as the feed line of electrical length βl [58]. The coupled susceptance is modified by the

In the case of a superconductor Z_o in (V.11) is implicitly taken as a function of temperature because of the kinetic inductance. For a low-loss line

$$Z_o \approx Z(0)\{(L_k(T) + L_e)\varepsilon(0)/[(L_k(0) + L_e)\varepsilon(T)]\}^{1/2} \qquad (V.12)$$

where $\varepsilon(T)$ is the temperature dependent effective permittivity, L_e is the magnetic or geometrical inductance, and $Z(0)$ is the characteristic impedance of the transmission line at T=0. Equation (V.12) is markedly different than the equation derived in [62] that expressed Z_o as being proportional to the ratio $\lambda(T)/\lambda(0)$. That expression was derived specifically for kinetic inductance delay lines, where $h \ll W$, and $t \ll \lambda$. In the situation considered here, L_k is not $\gg L_e$. Wheeler's incremental inductance rule, commonly used to characterize planar quasi-TEM transmission lines, only applies to shallow field penetration. Here, the inductance was derived from the imaginary part of the impedance calculated from the phenomenological loss equivalence method (PLE) [63]. This method has been shown to provide accurate results for both attenuation and phase velocity for quasi-TEM, normal and superconductor, transmission lines. It is summarized in section V.2.4.5.

Determining $\varepsilon(T)$ is not as straightforward but it can be estimated from [55] where resonant frequency versus temperature data were provided for a metallic conductor on $LaAlO_3$. $\Delta\varepsilon(T)$ was taken as -550 ppm/K which is an order of magnitude more severe than results disclosed in [56]. Still, the effect is subtle and the correction factor of (V.11) is dominated by L_k for resonators studied herein. The susceptance *B* can be evaluated as follows, for the general case when Z_o is not equal to Z_g. It is easy to show that $C_s = C_g + C_p$, $C_f = C_p[(C_p/C_g)^2 + 3C_p/C_g + 2]$, and $n^2 = C_s/(C_s + C_f)$, where C_g and C_p are the elements of the equivalent capacitive-pi representation from [64]. A series network can be made equivalent to a parallel network, and vice versa, at one frequency. Since we are interested in the behavior of the circuit of figure V.9 over a very narrow frequency range, the immittance looking towards the generator from the transformer was closely approximated by performing such a transformation. Let $K_1 = Z_o^2 Z_g\ [1 + \tan^2(\beta l)]/[Z_o^2 + Z_g^2\tan^2(\beta l)]$, $K_2 = Z_o(Z_o^2 - Z_g^2)\tan(\beta l)/[Z_o^2 + Z_g^2\tan^2(\beta l)]$, $K_3 = (\omega C_s K_2 - 1)/(\omega C_s)$, and finally

V.2.4.5. Surface Impedance

The propagation properties of a microwave signal through a transmission line are greatly influenced by the surface impedance of the conductor from which such a transmission line is made. The surface impedance is defined as,

$$Z_s=R_s+jX_s \qquad (V.13)$$

where R_s is the surface resistance and X_s is the surface reactance. For a good conductor the surface impedance is given by,

$$Z_s=(j\mu_o\omega/\sigma)^{1/2} \qquad (V.14)$$

where μ_o is the permeability of free space, ω is the angular frequency, and σ is the conductivity. It is evident from (V.13) and (V.14) that for a normal conductor, $R_s=X_s$, and that both parameters are proportional to the square root of the frequency. For a superconductor the conductivity is a complex quantity, $\sigma^*=\sigma_1-j\sigma_2$, and therefore R_s and X_s can be expressed in terms of σ_1 and σ_2 as,

$$R_s=R_N(\{[(\sigma_1/\sigma_2)^2+(\sigma_2/\sigma_N)^2]^{1/2}-(\sigma_2/\sigma_N)\}x[(\sigma_1/\sigma_N)^2+(\sigma_2/\sigma_N)^2]^{-1})^{1/2} \qquad (V.15)$$

where $R_N=(\mu_o\omega/2\sigma_N)^{1/2}$ is the surface resistance of the film at T_c. In the limit $\sigma_2>>\sigma_1$ (typically at $T<< T_c$, and for $\}h\omega/2\pi<<k_BT_c$) R_s and X_s are given by,

$$R_s\sim R_N(\sigma_1/\sigma_2)(\sigma_N/\sigma_2)^{1/2}=(\omega\mu_o)^2\lambda^3\sigma_1/2 \qquad (V.16)$$

$$X_s=\omega\mu_o\lambda=(\omega\mu_o/\sigma_2)^{1/2} \qquad (V.17)$$

where λ is the magnetic penetration depth. Note that in this limit the R_s of a superconductor increases as the square of the frequency. Figure V.11 shows R_s versus temperature for a YBCO (400 nm thick) on $LaAlO_3$ (254 μm thick) as measured using resonant cavity methods and power transmission method [48]. Note that both techniques give R_s values that decrease rapidly when the temperature falls below T_c and then level off at lower temperatures showing a residual surface resistance that changes very slowly with decreasing temperature.

An effective surface reactance (X_{eff}) can be defined in terms of the microwave power transmitted through superconducting thin films as follows [65],

$$X_{eff}=R_N\cosh(d/\lambda)\,|\,P_{Sxmitt}/P_{Nxmitt}\,|^{1/2} \qquad (V.18)$$

Figure V.12: Magnetic penetration depth vs. temperature for a laser-ablated thin film (200 nm) on $LaAlO_3$. The dashed lines represents a fit to the data using the temperature dependence for λ according to the two-fluid model and the solid line represents a fit to the data using the temperature dependence of λ according to the BCS theory in the clean limit.

$$Q_L = \omega_o RC(1+r)/(1+r+\kappa) = Q_O(1+r)/(1+r+\kappa) \qquad \text{(V.20)}$$

where κ is the coupling coefficient (or the ratio of coupled conductance to resonator conductance n^2R/Z_o) and r is the coupling loss. These terms can be determined from the reflection coefficient of the resonator. For small loss ($r<1$) the value of r can be calculated from the reflection coefficient far away from resonance according to:

$$r = (1-|\Gamma_\infty|)/(1+|\Gamma_\infty|) \qquad \text{(V.21)}$$

and the coupling coefficient can be found from the reflection coefficient at resonance by:

$$\kappa = [r-1 \pm |\Gamma_o|(r+1)] \div [\pm |\Gamma_o| - 1] \qquad \text{(V.22)}$$

The ambiguity in the sign of $|\Gamma_o|$ is resolved by considering whether the resonator is over- or under-coupled by inspection of the impedance locus on a Smith chart. The Γ vector traces a circle on the Smith chart of diameter $d=2\kappa/(\kappa+1)$. If $d>1$ the resonator is over-coupled and the plus sign is used. Conversely, if $d<1$ the resonator is under-coupled and the minus sign is used. Finally Q_L can be measured directly from the swept reflection coefficient trace using the familiar expression:

$$Q_L = f_0/(f_2 - f_1) \qquad \text{(V.23)}$$

where the frequency span $f_2 - f_1$ is the width of the reflection coefficient trace corresponding to magnitude:

$$\Gamma_{1/2} = 10 \log_{10} \{1/2[(r+\kappa-1)/(r+\kappa+1)]^2 + [(r-1)/(r+1)]^2\} \text{ dB} \qquad \text{(V.24)}$$

Then Q_O is obtained by substituting Q_L, r, and κ into (V.20).

The attenuation and phase velocity of superconducting microstriplines can be calculated using a theoretical approach such as the phenomenological loss equivalence (PLE) method [63]. The PLE method has been shown to be valid for either normal conductors or superconductors over a wide range of field penetrations. A planar quasi-TEM transmission line is approximated by an equivalent single strip having the same conductor loss. The geometry of the equivalent strip is obtained from the cross-sectional geometry of the original transmission line. For example, the internal impedance of a microstripline, assuming a perfect ground plane, is:

V. 3. FILTERS

V.3.1. Overview

Filters can be fabricated by arranging a given number of resonators in a pre-designed geometry, so as to allow the transmission (bandpass filter) or rejection (bandstop filter) of an electromagnetic signal within a specific frequency range. The low surface resistance (R_s) of HTS materials makes them attractive for the fabrication of filters where small physical size, minimum insertion loss and optimum frequency selectivity are design priorities. Numerouse studies of HTS-based filters with different geometry have been performed already [72-76]. For space communication applications the aforementioned features of HTS-based filters could prove to be advantageous in systems such as multiplexer filter banks. Typical satellite multiplexers use dual mode cavity or dielectric resonator filters that are large and heavy. As future advanced electronic systems for satellite communications become more complex, they will need even more filters requiring filter miniaturization without performance degradation. Microstrip filters using conventional conductors, which potentially can be used in filter banks, are small, but are too lossy for multiplexer applications. On the other hand, low temperature superconductors are less lossy but required more expensive coolants (e.g., liquid helium) or costly and sophisticated refrigeration systems. Microstrip filters using HTS films are just as small and lightweight but can perform with less power loss than their waveguide or coaxial counterparts and at a temperature that can be reached with low cost coolants (e.g., LN_2) or generally affordable cryocoolers (e.g., closed-cycle helium gas refrigerators). In this section we present several filters topologies that have been realized using HTS-technology.

V.3.2 Planar, Single-Mode Filters

Figure V.15 shows a schematic of a two-port C-band "edge-coupled", three-pole bandpass filter, with 4% bandwidth. The filter is made of three $\lambda_g/2$ microstrip linear resonators, where λ_g is the wavelength of the microwave signal propagating along the microstrip line, i.e., $\lambda_g=\lambda/(\varepsilon_{eff})^{1/2}$

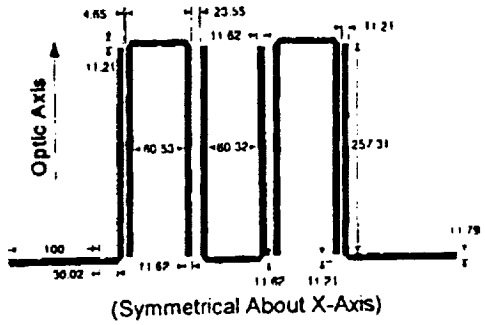

Figure V.17: Schematic configuration of a three-pole, C-band hairpin filter

Experimental data for this filter is shown in figure V.18. As can be seen, for the same center frequency, bandwidth, and number of poles this configuration reduce the overall length of the filter with respect to that of its edge-coupled filter counterpart.

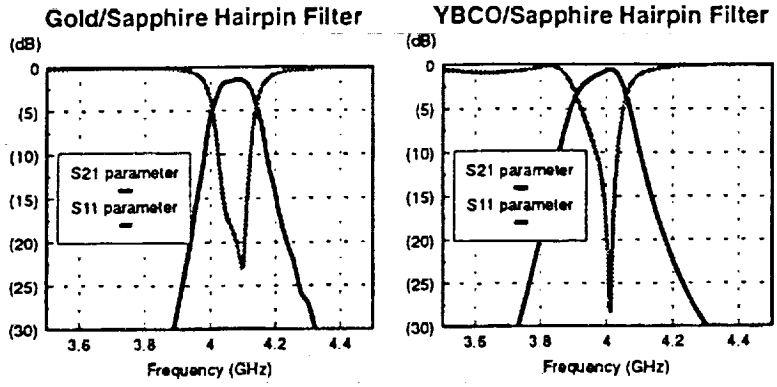

Figure V.18. Reflection and transmission parameters for the YBCO hairpin filters

small as possible. But, low ε_r substrates translate into bigger radiators and small h values reduce bandwidth and efficiency. In order to reduce R_{sw} the substrate thickness should be

$$h<c/[4f_c\sqrt{(\varepsilon_r-1)}] \qquad \text{(V.30)}$$

which defines the cutoff frequency (f_c) for the TE_1 mode of dielectric slab waveguide.

V.4.3 Antenna Arrays

Antenna arrays offer a straightforward way to enhance directivity, or if phase shifters are incorporated with the antenna elements the array can provide fast "inertialess" beam steering. The directivity of an array increases in proportion to the number of antenna elements (N) when the inter-element spacing is kept under a wavelength. In the case of a receive array, the signal-to-noise ratio scales with N since the signal is correlated but the noise contributed by each amplifier is not [83]. But the gain eventually decreases because of dissipation in the feed network. That is, beyond a certain array size at a given frequency, the gain peaks. A simple expression the gain of a manifold-fed array is

$$G \approx 10\log[4\pi(n+1)(m+1)s_h s_w/\lambda_o^2] - (\alpha/2)[(n+1)s_h + (m+1)s_v] \qquad \text{(V.31)}$$

where n (m) and s_h (s_v) are the number of elements and inter-element spacing in the horizontal (vertical) direction, respectively. The feed loss per unit length in dB is given by α. Capitalizing on the much lower surface resistance of superconductors, the gain maximum can be extended. That is, larger arrays with higher gains can be realized. In [84], a novel proximity coupled 12 GHz microstrip array was demonstrated. By using a parasitic array of elements on the quartz window of a cryostat, the superconducting driven elements were thermally isolated and broadband performance was achieved. A 64 element 30 GHz microstrip antenna array that used TlCaBaCuO HTS thin films has also been demonstrated [85]. The gain of the superconducting array at 77 K was found to be 4.7 dB higher than an identical gold version at 300 K. The antenna is shown in figure V. 19. A prototype GaAs MMIC low noise receiver array, designed to operate at 20 K, is under development at ≈100 GHz [86]. The array will be mounted in the focal plane of a Cassegrain parabolic reflector for radio astronomy applications.

For switching FETs, the Q_s^2 will degrade roughly as the square of frequency ω. Because of the low microwave losses of superconductors and the high ratio of normal surface resistance to surface resistance in the superconducting state, HTS switches have been investigated. A reflective microwave switch based on driving a small bridge into the normal state by locally exceeding the superconductor's critical temperature was demonstrated in [90] and a distributed Josephson inductance transmission line phase shifter was demonstrated in [91]. An electrically thin and narrow HTS switch of length *l* shunted between a microstrip signal path and a virtual short circuit formed by $\lambda/4$ radial stub has also been built [92]. The bridge can be electrically short or an integer multiple of half-wavelengths long to translate the virtual short to the microstrip line when superconducting. The bridge is driven normal by directly injecting dc current above the critical current through it. When the bridge is normal, the short is "disconnected" from the transmission line. In order to minimize insertion loss and maximize isolation, *l* was set to $\lambda/2$ and the bridge was about $\lambda_L/2$ thick to increase the impedance looking toward the stub in the normal state. A Q_s^2 approaching 100 at 10 GHz has been measured. A switched line phase shifter based on this type of switch is shown in figure V.20.

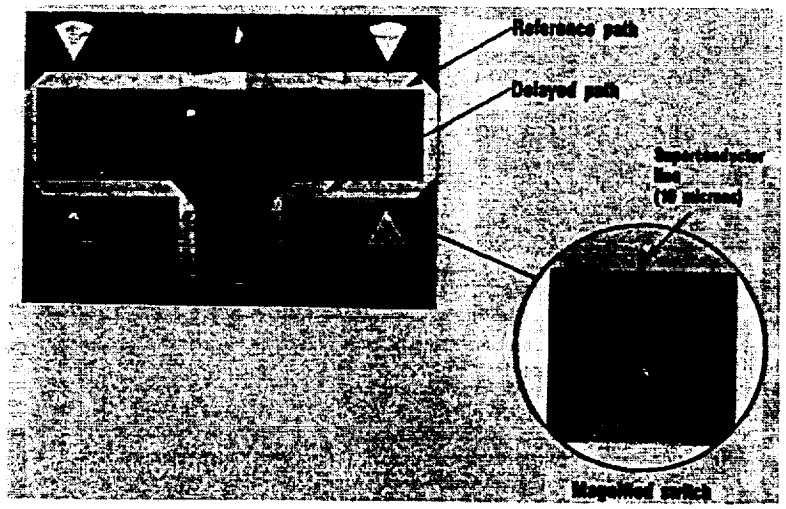

Fig. V.20 Switched line phase shifter on ZrO_2:Y. The phase shifter circuit is about 5 mm long.

where V_o is the peak amplitude of the carrier, ω_o is the angular frequency, $\varepsilon(t)$ is the amplitude noise term, and $\varphi(t)$ is the phase noise term. For $|\varepsilon(t)| << V_o$, and $|\varphi(t)| << 1$ rad,

$$V(t) \approx V_o \sin(\omega_o t) + V_o \varphi(t) \cos(\omega_o t) + \varepsilon(t)\sin(\omega_o t) \qquad (V.34)$$

where the first term is the carrier, the second term represents the phase noise, and the third term represents the amplitude noise. Since the last two terms produce deviations from the ideal sinusoidal oscillation, they can be regarded as modulating the carrier. In practice, the phase noise manifests itself as continuous energy sidebands around the carrier in the frequency domain. For the usual case when the phase noise dominates (i.e., the amplitude noise is insignificant), the spectrum around the carrier is symmetrical.

The spectral density of phase fluctuations can be attributed to the following factors. There is a thermal noise floor associated with the kinetic energy of electrons. Thermal noise is broadband and essentially flat with frequency (ω). It is often called "white" noise because of this behavior (i.e. white light is broadband). Active devices also exhibit a noise characteristic which scales as ω^{-1}. This noise is called "flicker" noise, evidently because of historical observations of plate current in vacuum tubes. In the case of semiconductors, this fundamental physical phenomenon has been attributed to the generation and recombination of carriers at semiconductor surfaces, and the capture and release of carriers at electrically active defects or traps. Furthermore, in a feedback oscillator, a phase change anywhere in the loop translates into a frequency change. That is, the phase modulation is converted directly into frequency modulation (i.e. frequency being the time derivative of phase). The power spectral density (rad^2/Hz) of phase fluctuations is proportional to the root mean square (rms) phase deviation squared. The net result is that spectral slope of the white and flicker noise becomes twice as steep. A common way to express phase noise is the ratio of single sideband noise power per Hertz to the carrier power at a specific offset frequency. Following Leeson [93], a simple model can be summarized as follows. The power spectral density, as a function of offset

$$P_B := \frac{1}{4\cdot\sqrt{2\cdot\pi\cdot\sigma^2}}\cdot\int_{-\frac{\pi}{4}}^{\frac{\pi}{4}}\left[\operatorname{erfc}\cdot\left[\left(\frac{E_b}{N_o}\right)^{\frac{1}{2}}\cdot\sqrt{2}\cdot\sin\left(\frac{\pi}{4}-\theta\right)\right]+\operatorname{erfc}\cdot\left[\left(\frac{E_b}{N_o}\right)^{\frac{1}{2}}\cdot\sqrt{2}\cdot\cos\left(\frac{\pi}{4}-\theta\right)\right]\right]\cdot e^{\frac{-\theta^2}{2\cdot\sigma^2}}\,d\theta$$

(V.37)

In order to minimize BER degradation, high Q resonators and low ω^{-1} noise transistors are required. At frequencies below a few hundred MHz, quartz crystal oscillators provide extremely stable sources. At low microwave frequencies, sources are often implemented by multiplying up from a crystal source. But the phase noise degrades according to (V.35). The efficiency is also poor and cost is an issue. Metal cavities are often used as the stabilizing element but are bulky and costly. The dielectric resonator oscillator (DRO) has become a practical compromise at high microwave frequencies in terms of cost, size, and performance. Their popularity has grown with the development of very low loss tangent, thermally stable ceramics. Still, there is a tremendous interest in lower cost, miniature, tunable oscillators. Despite the lower Q of MMIC chips, several types of integrated oscillators have been successfully developed. Transistor oscillators have been realized using both MESFET and bipolar devices. GaAs MESFETs can be used at very high frequencies but exhibit relatively poor baseband noise performance. Bipolar Si transistors have superior noise behavior but are limited to a frequency range of about 20 GHz. Recently, InAlAs/InGaAs, AlGaAs/GaAs, and InGaAs/InP MMIC HBT based oscillators have been demonstrated with excellent performance from Ku- through Ka-band [97-99]. At 26 GHz, a phase noise of –80 dBC/Hz at 100 kHz offset, with a conversion efficiency of about 10% has been reported.

V.5.3 Tunable Oscillators

Planar superconducting microstrip resonator oscillators have also been developed with excellent characteristics [100]. A cryogenic voltage controlled oscillator (VCO) has also been developed at Ku-band [17]. The oscillator schematic is shown in figure V.21. The S-parameters of the 0.25 μm PHEMT were measured at 77 K by immersing the

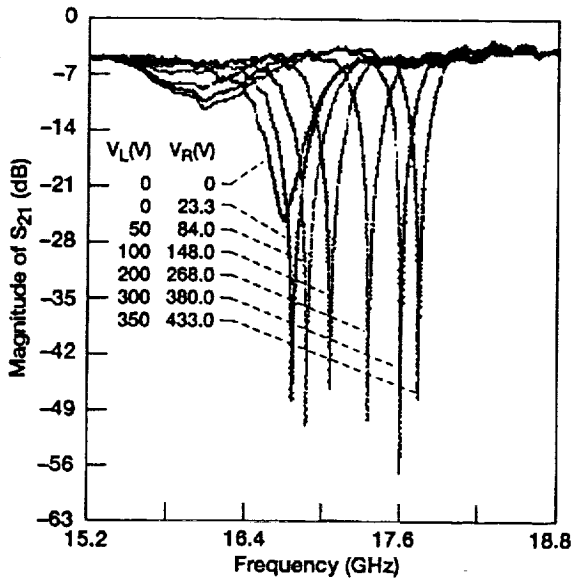

Fig. V.22 Tuning of a side-coupled 50 Ω ring resonator corresponding to the VCO of Fig. V.21. The voltages correspond to the dc bias between the ring (V_R) and microstrip line (V_L). During VCO operation, the microstrip line is kept at dc ground.

Table V.II State-of-the-Art Tunable Resonator Comparison

RESONATOR TYPE	TUNING METHOD	TUNING RANGE	Q	TEMPERATURE CONTROL
Varactor	Electronic	One Octave	10-50	Ovenized
YIG	Magnetic	One Decade	500-3000	Ovenized
DRO	Mechanical	10%	5000-30000	Stable
Cavity	Mechanical	<One Octave	200-1000	Ovenized
HTS/Ferroelectric	Electronic	7%	3000-6000	Cryocooler

contact deposition annealing. It was also observed that contact strength was inversely proportional to the amount of silver in the contact. In-situ deposited gold contacts were the strongest observed. A copper microstrip X-band GaAs FET oscillator for use in a Josephson voltage standard demonstrated a 22 dB improvement in phase noise at 4.2 K compared to room temperature operation [105]. A 36.5 GHz oscillator based on a sapphire disk resonator shielded by two HTS ground planes provided a 20 dB improvement in phase noise over a conventional room temperature dielectric resonator oscillator [106]. At 77 K a loaded Q of 59,000 was obtained. One implementation of an HTS-sapphire-HTS resonator is shown in figure V.23 [107]. The surface resistance of the $Tl_2Ba_2CaCu_2O_8$ films was 130 $\mu\Omega$ at 77K and 10 GHz. Around 90 K unloaded Qs of $>10^6$ were reported along with circulating power handling capability of 2 kW.

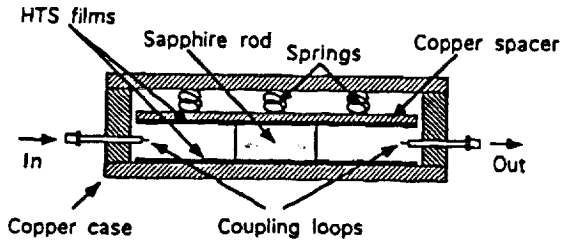

Figure V.23 An HTS-Sapphire-HTS resonator [107]

For this structure, the relationship between loaded and unloaded Q is as follows.

$$Q_o = Q_L(1 + \beta_1 + \beta_2) \qquad \text{(V.38)}$$

where the coupling coefficients at the input (β_1) and output (β_2) ports are calculated according to

$$\beta_1 = (1 - S_{11})/(S_{11} + S_{22}) \qquad \text{(V.39)}$$

$$\beta_2 = (1 - S_{22})/(S_{11} + S_{22}) \qquad \text{(V.40)}$$

where the S-parameters are measured at the resonant frequency.

Cooled pseudomorphic HEMTs were found to be well suited to cryogenic oscillators as well [108]. While room temperature performance is mediocre, below 110 K the PHEMTs are generally free of collapse and exhibit excellent generation-recombination noise performance. Phase noise improvements of 10 to 15 dB have been

V.6 Hybrid Superconductor/Semiconductor Receiver "Front Ends"

V.6.1 Overview

Low noise parametric amplifiers (paramps) have been used for ground stations and satellite transponders from L-band through Ku-band. Since the introduction of the GaAs MESFET in the 1970's and the more recent derivative, a high electron mobility transistor (HEMT), cooling has been used to deliver performance that has steadily approached that of paramps [111-113]. In order to reduce noise that is thermal in origin and achieve higher frequency operation, the FET's transconductance to gate-to-source capacitance (g_m/C_{gs}) ratio must increase. Reducing gate length is one way. But since the transconductance is proportional to carrier mobility, which is a function of electric field, temperature and impurity concentration, cooling also offers significant advantages. Velocity overshoot effects for short gate lengths are also more pronounced at very cold temperatures. When pure GaAs is cooled to 77 K, the electron velocity increases to $\approx 2.4 \times 10^7$ cm/s, compared to $\approx 10^7$ cm/s at room temperature for a channel doped at $10^{17}/cm^3$. The HEMT's superior noise performance is due to much higher mobility and consequently much higher g_m. Also, the improvement upon cooling is more rapid than a conventional MESFET.

Communications receivers often require a preselect filter ahead of the low noise amplifier (LNA) to either suppress unwanted signals in a heavy interference environment or to limit noise input to sensitive, wide band LNAs that could swamp the amplifier and cause nonlinear effects. The insertion loss of the filter has a dramatic impact on the overall system noise temperature (T_{sys}). This is because losses (L_F) between the antenna terminals and the LNA increase T_{sys} according to the well known cascade noise formula:

$$T_{sys} = T_A + T_{AP}(1/\varepsilon_A - 1) + (L_F - 1)T_{FP} + L_F T_{REC} \qquad (V.41)$$

where T_A is the antenna temperature given by [114]:

$$T_A = 1/4\pi \int D(\theta,\phi)T_b(\theta,\phi)d\Omega \qquad (V.42)$$

gain-to-noise temperature ratio (G/T) with a room temperature receiver, the dish would have to be 1.8 m in diameter with a 0.6 degree beamwidth. The smaller cryoterminal produces a 1.3 degree beamwidth, simplifying tracking requirements.

V.6.2 HEMT Amplifiers

The HEMT represents an evolutionary improvement to the workhorse GaAs FET of the microwave industry [117]. In a conventional FET, carriers flow through the doped channel layer and experience substantial scattering. In a HEMT, a potential well is created on the undoped GaAs side of an AlGaAs/GaAs interface. Since the carriers travel through the undoped GaAs, impurity scattering is reduced and mobility and velocity are greatly increased. The channel mobilities for a HEMT and a FET at 77 K are roughly 60,000 cm^2/Vs and 10,000 cm^2/Vs, respectively, for sheet carrier densities near $10^{12}/cm^2$.

Unfortunately, at low temperatures HEMTs suffer from the formation of deep electron traps in the $Al_xGa_{1-x}As$ layer, leading to collapse of the I-V characteristic, for high mole fraction (x>0.2) Al. The use of InGaAs as the low bandgap material, instead of GaAs, has alleviated this problem. Because of its lower bandgap, a lower Al mole fraction can be used while preserving the conduction band discontinuity [118]. The strain (compression) from the ≈1% lattice mismatch between the GaAs buffer and the InGaAs is accommodated elastically for thin (≈ 200 A) layers, hence the name pseudomorphic HEMT. Persistent photoconductivity effects and the impact of illumination on device behavior at cryogenic temperatures have also been investigated for various structures [119-122]. At room temperature, most deep donors are ionized. Upon cooling with positive gate voltage, carriers can be trapped and neutralize deep donors. Sometimes, illumination (e.g. LEDs mounted above the HEMT) is used to prevent the IV collapse and compensate for the threshold voltage shift.

Ultra-low noise amplifiers from 12 to 110 GHz based on InGaAs/InAlAs/InP HEMTs have demonstrated the highest cutoff frequencies, highest maximum oscillation frequencies, and the lowest noise figure from any three terminal semiconductor device [123-126]. The higher conduction band discontinuity at the InGaAs and InAlAs interface and improved transport properties in the InGaAs channel yield higher transconductance

empirical approach was developed by Fukui [129] that relates F_{min} at a particular frequency to G_{gs}, g_m, and the gate and source resistance r_g and r_s, respectively. The expression for the minimum noise figure is given as

$$F_{min} \approx 1 + KC_{gs}\omega[(r_g + r_s)/g_m]^{1/2} \qquad (V.46)$$

where K is empirically derived (≈ 2.5) and depends on material quality. Reducing C_{gs} and increasing g_m clearly impact F_{min}. This expression is an approximation to the comprehensive analysis of Pucel, Haus, and Statz [130]. It neglects induced gate noise and high frequency effects. A distributed model, improving upon the lumped element circuit model, was presented in [131]. That model takes into account electrode coupling and distributed phase effects. A faster increase in noise figure with frequency is predicted than the Fukui model. A review of noise theory and modeling, along with a comparison of MESFET and HEMT noise performance, was presented in [132]. Because of the correlation between drain and gate noise sources, gate noise is partially subtracted from drain noise, as alluded to above. The HEMT's superior noise performance is attributed to the correlation coefficient and the HEMTs higher cutoff frequency. And, HEMTs have a reduced sensitivity to source impedance changes, resulting in wider bandwidth low noise performance [133].

A noise model was described in [134] that provided expressions for the minimum noise temperature (T_{min}), the optimum source impedance (Z_{opt}), the noise conductance (g_n), and source impedance minimizing noise measure (Z^M_{opt}). These terms were related to the elements of an equivalent circuit and two frequency independent constants, the equivalent temperatures T_g and T_d of the intrinsic gate resistance r_{gs} and drain conductance g_{ds}, respectively. Knowledge of the equivalent temperatures T_d and T_g and the equivalent circuit element values at a certain temperature allows the computation of the noise parameters at any frequency. The expression for the noise temperature of a two-port driven by a generator with impedance Z_g is

$$T_n = T_{min} + T_o(g_n/R_g)|Z_g - Z_{opt}|^2 \qquad (V.47)$$

and the definition of noise measure is

programmable termination based on p-i-n diodes. By changing the bias on the diodes, radial coverage of the Smith chart is obtained while varying the frequency provides angular coverage. Noise is injected between the input port and the termination through a coupler.

The design and operation of cryogenic on-wafer probe stations has been discussed in the literature [138-141]. The 40 GHz probe station described in [141] uses an open cycle cooling system that can be cooled with either liquid nitrogen or liquid helium. The cryoprobe station chamber is shown in figure V.25. The chamber contains the 2.5 cm by 5 cm sample stage, cooling head of the refrigerator, temperature sensors and flexible coplanar microwave probes. An open cycle system was chosen to reduce microphonics induced noise and to reduce vibrations that could affect the delicate probe contacts. The sample stage was machined from a 7.5 mm thick piece of oxygen-free, high conductivity (OFHC) copper. Precision manipulators with 2.5 μm resolution can move the probes over the entire sample stage using metal bellows coupling system. The minimum achievable temperatures for liquid nitrogen and liquid helium coolants are 80 K and 37 K, respectively.

expended on the thermal design to minimize heat leaks, internal power dissipation, and thermal mass. For example, commercially available coaxial lines for RF/IF input and output connections are usually not acceptable because of their high thermal conductivity. One solution is to take advantage of the skin depth at high frequencies. Gold plating low thermal conductivity material (e.g. stainless steel) can provide low attenuation and reduced heat conduction. For such a 50Ω coaxial line a heat load of perhaps 200 mW with an insertion loss of 0.5 to 1 dB is possible. Thermal breaks in waveguide have also been used. Another potential problem is mechanical incompatibility between hybrid circuits on ceramic carriers and the module package. Thin film microstrip circuits on alumina have been successfully bonded to kovar carriers with silver-filled epoxy and repeatedly cycled to 77K. The thermal expansion coefficients of alumina and kovar at room temperature are about 7 ppm and 6 ppm, respectively. Indium foil, about 25 μm thick, can be sandwiched between the kovar carrier and the housing to improve heat sinking. Table V.IV is a partial listing of the properties of materials that are of interest to cryogenic electronics applications [151-153]. Circuit designs also stress efficiency to minimize waste heat. For example, the local oscillator in a downconverter can typically provide only about 10% dc-to-rf conversion efficiency. A typical mixer may require 10 mW or so of oscillator drive to minimize conversion loss and noise figure. While there may be no great benefit to cooling the mixer when it is preceded by an LNA, it is desirable to place it in the same package for the sake of integration, and doing so saves one coaxial I/O. Consequently, a mixer/oscillator sub-module could easily dissipate 100 mW. Given a state-of-the-art compact and reliable Stirling cycle or pulse-tube cryocooler with perhaps 1 W of lift at 77 K, this is intolerable. A singly-balanced mixer has been demonstrated that had a conversion loss of 3.2 dB

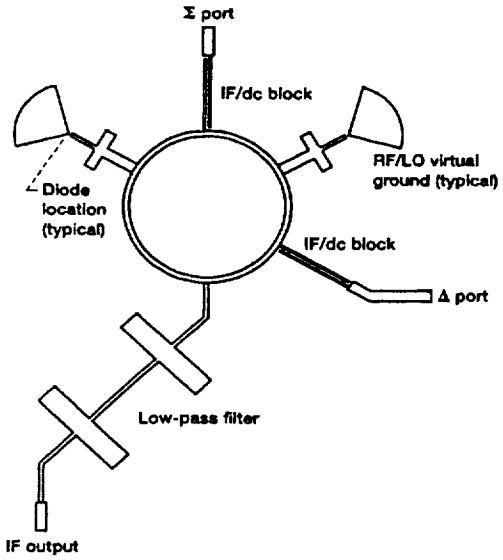

Figure V.26 Layout of the matched mixer. The circuit is 1.9 cm wide and 2.5 cm long.

It is well known that the I-V characteristic, particularly the ideality factor η and the barrier height ϕ_b, are strongly influenced by operating temperature. A precise equivalent circuit representing the diode, as well as an accurate description of its band structure, is required to optimize the mixer design. The calculated energy band diagram of the Si diodes, which were arsenic doped with a donor concentration of $N_D=1.2x10^{17}/cm^3$, is shown in figure V.27a. The flatband potential, ϕ_{bi}, is the difference between the barrier height and the difference in potential between the Fermi level and the conduction band edge. The quasi-static circuit model, extracted from cryogenic dc and microwave measurements, is shown in figure V.27b. It consists of the

approximation that deteriorates as forward voltage approaches flatband, yet it is widely used in mixer analysis. A more exact numerical analysis, indicating a much less dynamic change in C_j near flatband, was reported in [157]. Experimental data on the behavior of $C_j(V_j)$ at 77 K based on a microwave measurement and modeling technique was presented in [158]. The capacitance was found to increase more slowly than predicted and C_{jmax} occurred in advance of flatband. Expectations of degraded intrinsic conversion loss upon cooling are overly pessimistic.

The space qualified receiver downconverter developed in [150] for the High Temperature Superconductivity Space Experiment [159] is shown in figure V.28. It consists of a four-pole HTS preselect filter, a two-stage GaAs HEMT LNA, a singly-balanced hybrid ring mixer, and an oscillator stabilized with a $\lambda/2$ linear resonator. The insertion loss of the filter was about 0.25 dB across 7.2 to 7.4 GHz, about 0.5 dB better than a copper version also at 77 K. The LNA noise temperature was about 21 K with a gain of 28 dB. The 8.4 GHz GaAs MESFET oscillator used a Y-Ba-Cu-O on $LaAlO_3$ resonator that had an unloaded Q of about 6000. A qualification receiver had an overall noise temperature of 50 K when operated at 77 K with a total power consumption of 70 mW.

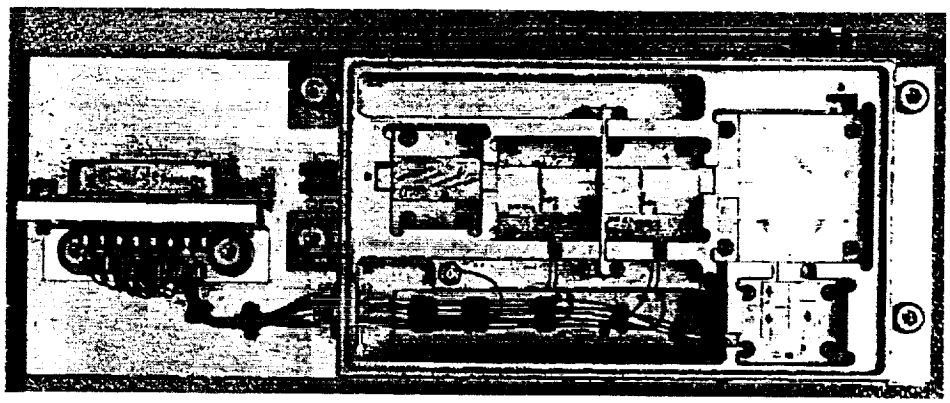

Figure V.28 Space qualified X-band receiver downconverter prior to hermetic sealing. The package measures about 10 cm across.

References

1. J. G. Bednorz and K. A. Mueller, Possible High-T_c Superconductivity in the Ba-La-Cu-O System, Z. Physics B 64, 189-193 (1986).
2. M. K. Wu, J. R. Ashburn, C. J. Torng, P. H. Hor, R. L. Meng, L. Gao, Z. J. Huang, Y. Q. Wang, and C. W. Chu, Superconductivity at 93 K in a New Mixed-Phase Y-Ba-Cu-O System at Ambient Pressure, Phys. Rev. Lett. 58, 908-910 (1987).
3. H. Maeda, Y. Tanaka, M. Fukutomi, and T. Asano, A New High-T_c Oxide Superconductor Without a Rare Earth Element, Jpn. J. Appl. Phys. 27, L209-L210 (1988).
4. Z. Z. Sheng and A. M. Hermann, Bulk Superconductivity at 120 K in the Tl-Ca-Ba-Cu-O System, Nature 332, 138-139 (1988).
5. S. N. Putilin, E. V. Antipov, O. Chmaissem, and M. Marezio, *Nature*, **362**, 223 (1993).
6. R. I. Meng, Y. Y. Sun, J. Kulik, Z. J. Huang, F. Chen, Y. Y. Xue, and C. W. Chu, *Physica C*, **214**, 307-312 (1993).
7. N. Klein, G. Mueller, H. Piel, B. Roas, L. Schultz, U. Klein, and M. Peiniger, *Millimeter Wave Surface Resistance of Epitaxially Grown $YBa_2Cu_3O_{7-\delta}$ Thin Films*, **Appl. Phys. Lett. 54**, 757-759 (1989).
8. N. Newman, K. Char, S. M. Garrison, R. W. Barton, R. C. Taber, C. B. Eom, T. H. Geballe, and B. Wilkens, Appl. Phys. Lett. 57, 520 (1990).
9. F. A. Miranda, W. L. Gordon, K. B. Bhasin, and J. D. Warner, Appl. Phys. Lett. 57, 1058 (1990).
10. S. H. Talisa, M. A. Janocko, C. Moskowitz, J. Talvacchio, J. F. Billing, R. Brown, D. C. Buck, C. K. Jones, B. R. McAvoy, G. R. Wagner, and D. H. Watt, Low- and High Temperature Superconducting Microwave Filters, IEEE Trans. Microwave Theo. Tech., 39, 1448-1454 (1991).
11. F. A. Miranda, K. B. Bhasin, K-S. Kong, T. Itoh, and M. A. Stan, Conductor-Backed Coplanar Waveguide Resonators of $YBa_2Cu_3O_{7-d}$ on $LaAlO_3$, IEEE Microwave Guided Wave Lett. 2, 287-288 (1992).

24. J. Talvacchio, M. G. Forrester, and A. I. Braginski, *Photodetection with High-Tc Superconducting Films*, Science and Technology of Thin Film Superconductors, eds. R. D. McConnell and S. A. Wolf, (Plenum 1990).

25. B. Y. Tsaur, M. S. Dilorio, A. J. Strauss, *Preparation of Superconducting YBa2Cu3Ox Thin Films by Oxygen Annealing of Multilayer Metals Films*, **Appl. Phys. Lett. 51**, 858-860 (1987).

26. P. M. Mankiewich, J. H. Scoefield, W. J. Skocpol, R. E. Howard, A. H. Dayen, and E. Good, *Reproducible Technique for Fabrication of Thin Films of High Transition Temperature Superconductors*, **Appl. Phys. Lett. 51**, 1753-1755 (1987).

27. S. W. Chan, B. G. Bagley, L. H. Greene, M. Giroud, W. L. Feldman, K. R. Jenken, and B. J. Wilkins, *Effect of the Post-deposition Processing Ambient on the Preparation of Superconducting $YBa_2Cu_3O_{7-x}$ Coevaporated Thin Films Using a BaF_2 Source*, **Appl. Phys. Lett. 53,** 1443-1445 (1988).

28. J. R. Phillips, J. W. Mayer, J. A. Martin, and M. Nastasi, *Vapor-deposited Superconducting $YBa_2Cu_3O_{7-\delta}$ Lines: Effect of Thickness and Width on Morphology*, **Appl. Phys. Lett. 56,** 1374-1376 (1990).

29. M. A. M. Gijs and R. J. E. Jansen, *Microwave Response of YBaCuO Thin Film Dayem Bridges*, **Appl. Phys. Lett. 56**, 1484-1486 (1990).

30. T. S. Kalkur, R. Kwor, S. Jernigan, and R. Smith, *Co-evaporated Bi-Sr-Ca-Cu-Oxide Superconducting Films and Their Patterning*, presented at the conference, **Sci. Technol. Of Thin Films Supercond.**, Colorado Springs, CO., Nov. 14-18, 1988.

31. R. C. West, ed., *CRC Handbook of Chemestry and Physics*, **69th edition**, CRC Press, Inc. (1988-1989).

32. S. Withington, *Cryogenic Performance of Microstrip Substrates*, Elect. Lett., Vol. 19, pp. 887-888, Oct., 1983.

33. R.R. Romanofsky, J.C. Martinez, B.J. Viergutz, and K.B. Bhasin, *Ka-Band Propagation Characteristics of Microstriplines on GaAs Substrates at Cryogenic Temperatures*, Micro. Optical Tech. Lett., Vol. 3, No. 4, pp. 117-119, April, 1990.

47. Y. Yoshisato, A. Takeoka, T. Ikemachi, K. Niki, T. Yokoo, S. Nakano, and Y. Kuwano, **Jpn. J. Appl. Phys. 29**, 1080 (1990).

48. F. A. Miranda, W. L. Gordon, K. B. Bhasin, V. O. Heinen, and J. D. Warner, *Microwave Properties of $YBa_2Cu_3O_{7-\delta}$ High-Transition-Temperature Superconducting Thin Films Measured by the Power Transmission Method*, **J. Appl. Phys. 70**, 5450-5462 (1991).

49. D. C. Mattis and John Bardeen, **Phys. Rev. 111**, 412 (1958).

50. L.C. Hebel and C. P. Slichter, **Phys. Rev. 107**, 901 (1957);**113**, 1504 (1959).

51. W. W. Warren, R. E. Walstedt, G. F. Brennert, G. P. Espinosa, and J. P. Rameika, **Phys. Rev. Lett. 59**, 1860 (1987).

52. J. C. Gorter and H. B. Casimir, *The Thermodynamics of the Superconducting State*, **Physik. Z. 35**, 963-966 (1934).

53. W. H. Henkels and C. J. Kircher, "Penetration Depth Measurements on Type II Superconducting Films," **IEEE Trans. Magn.**, vol. 13, No.1, pp. 63-66, Jan. 1977.

54. S. M. Anlage, B. W. Langley, H. J. Snortland, C. B. Eom, T. H. Geballe, and M. R.Beasley, Magnetic Penetration Depth Measurements with the Microstrip Resonator Technique, J. Superconductivity, Vol. 3, No. 3, pp. 311-316, 1990.

55. C. M. Chorey, K. S. Kong, K. B. Bhasin, J. D. Warner, T. Itoh, YBCO Superconducting Ring Resonators at Millimeter-Wave Frequencies," IEEE Trans. MTT, Vol. 39, No. 9, pp. 1480-1487, Sep. 1991.

56. A.A. Valenzuela, G. Solkner, J. Kessler, and P. Russer, "Microwave Characterization of Structured $YBa_2Cu_3O_{7-}$ Thin Films," in *Synthesis and Characterization of High-Temperature Superconductors*, J. J. Pouch et al., Eds. Trans Tech Publications Ltd., 1993, pp. 349-372.

57. F A. Miranda, Microwave Properties of Tl-Ba-Ca-Cu-O Thin Films, Supercond. Sci. Technol., Vol 6, pp. 605-613, 1993.

58. R.R. Romanofsky, "Correction Factor for Determining the London Penetration Depth from Strip Resonators," **IEEE Trans. Appl. Superconductivity**, Vol. 8, No. 3 (1998).

59. M. Maeda, An Analysis of Gap in Microstrip Transmission Lines, IEEE Trans. MTT, Vol. 20, No. 6, pp. 390-396, Jun. 1972.

Temperature Microwave Filters, **IEEE Trans. Microwave Theory Techs., Vol MTT-39**, 1448-1454 (1991).

73. W. G. Lyons, R. R. Bonetti, A. E. Williams, P. M. Mankiewich, M. L. O'Malley, J. M. Hamm, A. C. Anderson, R. S. Withers, A. Meulenberg, and R. E. Howard, *High-Tc Superconductive Microwave Filters*, **IEEE Trans. Magn., MAG-27** 2537-2539 (1991).
74. A. Enokihara, K. Setsune, K. Wasa, M. Sagawa, and M. Makimoto, *High-Tc Bandpass Filter Using Miniaturized Microstrip Hairpin Resonators*, **Electron. Lett. 28**, 1925-1927 (1992).
75. F. Suginosita, K. Imai, N. Yazawa, K. Suzuki, S.Fujino, T. Takenada, and K. Nakao, *13.3 GHz YBCO Microstrip Bandpass Filter*, **Electron. Lett. 28**, 355-357 (1992).
76. F. A. Miranda, S. S. Toncich, and K. B. Bhasin, *Performance of Two-Pole Bandpass Filters Photodefined on Doubled-Sided Y-Ba-Cu-O and Tl-Ba-Ca-Cu-O Thin Films*, **Microwave Opt. Tech. Lett. 6**, 752-755 (1993).
77. R.J. Dinger, Some potential Antenna Applications of High Temperature Superconductors, Journal of Superconductivity, Vol.3, No. 3, pp. 287-296, 1990.
78. J.T. Williams and S.A. Long, High Temperature Superconductors and Their Application in Passive Antenna Systems, IEEE Ant. Propagation Mag., pp. 7-18, Aug. 1990.
79. R.C. Hansen, Superconducting Antennas, IEEE Trans. Aerospace and Electronic Systems, Vol. 26, No. 2, pp. 345-355, Mar., 1990.
80. S. Khamas, G.G. Cook S.P. Kingsley, and R.C. Woods, Significance of matching Networks in Enhanced Performance of Small Antennas when Supercooled, Electronics Letters, Vol. 26, No. 10, pp. 654-655, May, 1990.
81. M.J. Lancaster, T.S.M. Maclean, J. Niblett, N. McN.Alford, and T.W. Button, YBCO Thick Film Loop Antenna and Matching Network, IEEE Trans. Applied Superconductivity, Vol. 3, No. 1 pp. 2903, March, 1993.
82. K. Itoh O. Ishii, Y. Nagai, N. Suzuki, Y. Kimachi, and O. Michikami, High-Tc Superconducting Small Antennas, IEEE Trans. Applied Superconductivity, Vol. 3, No.1, pp. 2836, March, 1993.
83. M.DeLisio, R.M. Weikle, D.B. Rutledge, Element Efficiency and noise in Grid Arrays, IEEE Trans. MTT, Vol 46, no. 11, pp 1949-1955, Nov. 1998.

108.O.Llopis, R. Plana, H.Laurent, and J. Graffeuil, Phase Noise in Cryogenic Microwave HEMT and MESFET Oscillators, IEEE Trans. MTT, Vol. 41, No. 3, pp. 369-374, Mar., 1993.

109.R.C. Taber and C.A. Flory, Microwave Oscillator Incorporating Cryogenic Sapphire Dielectric Resonators, IEEE Trans. Ultra., Ferro. And Freq. Cont., Vol. 42, No.1, pp. 111-121.

110.R.C. Almar and M.S. Cavin, Low g-Sensitivity Fixed-Frequency Oscillators, Micro. Jour., pp. 8-96, Feb. 1995.

111.D.R. Williams, W. Lum, S. Weinreb, L-Band Cryogenically Cooled GaAs FET Amplifier, Microwave Journal, pp. 73-76, Oct. 1980.

112.B. Vowinkel, Cryogenic 2-4 GHz FET Amplifier, Electronic Lett., Vol. 16, No. 19, pp730-731, Sept. 1980.

113.G. Tomassetti, S.Weinreb, Wellington, Electronics Lett., Vol. 17, No. 25, pp. 949-951, Dec. 1981.

114.K.M. Lambert and R.C. Rudduck, Calculation and Verification of Antenna Temperature for Earth-Based Reflector Antennas, Radio Science, Vol. 27, No. 1, pp. 23-30, Jan. 1992.

115.J.M. Budinger, G. Fujikawa, R.Kunath N.T. Nguyen, R.R.Romanofsky, and R.L. Spence, Direct Data Distribution from Low-Earth Orbit, IEEE Int'l. Conf. On Communications, Montreal, June, 1997, NASA TM-107438.

116.C. Raquet Private Communication, NASA Glenn Research Center, Feb. 1999

117.P.M. Smith and A.W. Swanson, HEMTs-Low Noise and Power Transistors for 1 to 100 GHz, Applied Microwave, pp. 63-72, May 1989.

118.A.W. Swanson, The Pseudomorphic HEMT, Microwaves & RF, pp. 139-150, March 1989.

119.C.C. Yang, B. Nelson, W. Jones, and B. Allen, A Cryogenically Cooled Wide-Band HEMT MMIC Low-Noise Amplifier, IEEE Microwave and Guided Wave Letters, Vo 2, No. 2, pp. 5860, 1992.

120.Y-J Chan, D. Pavlidis, M. Razeghi, F.Omnes, $Ga_{0.51}In_{0.49}P$/GaAs HEMTs Exhibiting Good Electrical Performance at Cryogenic Temperatures, IEEE Trans. Electron evices, Vol. 37, No. 10, pp.2141-2146, 1990.

142.Z-Y. Shen, P. Pang, C. Wilker, D.B. Laubacher, W.L. Holstein, C.F. Carter, and M. Adlerstein, High Tc Superconductor and III-V Solid State Microwave Hybrid Circuits, IEEE rans. Applied Superconductivity, Vol. 3, No. 1, pp. 2832-2835, 1993.

143.B. Vowinkel, K. Gruner, H. Suss, and W. Reinert, Cryogenic All Solid-State Millimeter-Wave Receivers for Airborne Radiometry, IEEE MTT-S Digest, pp. 566-568, 1983.

144.P. Piironen, J. Mallat, A. Raisanen, A Space Qualified Low-Noise 22 GHz Receiver with High Phase Stability for VLBI-Measurements, IEEE MTT-S Digest, pp. 1089-1092, 1994.

145.W.A. Phillips, D. Jedamzik, K. Lamacraft, S. Zammattio, R.B. Greed, S.J. Hedges, P.R. Whitehead, B.F. Nicholson, T.W. Button, P.A. Smith, N. McN. Alford, N. Peters, and J. Grier, An Integrated 11 GHz Cryogenic Downconverter, 1994.

146.O.P. Koistinen, H.T. Valmu, A. Raisanen, V.F. Vdovin, Y.A. Dryagin, and I.V. Lapkin, A 110 GHz Ozone Radiometer with a Cryogenic Planar Schottky Mixer, IEEE Trans. MTT, Vol. 41, No. 12, pp. 2232-2235, Dec 1993.

147.R. Lai, J.J. Bautista, B. Fujiwara, K.L. Tan, G.I. Ng, R.M Dia, D. Streit, P.H. Liu, A. Freudenthal, J. laskar, and M.W. Pospieszalski, An Ultra-Low Noise cryogenic Ka-Band InGaAs/InAlAs/InP HEMT front-End receiver, IEEE Microwave and Guided Wave Letters, Vol. 4, No. 10, pp. 329-331, 1994.

148.R. Romanofsky, K. Bhasin, A Downey, C. Jackson, A. Silver, H. Javadi, Integrated Cryogenic Satellite Communications Cross-Link Receiver Experiment, 16th Int'l. Comm. Sat. Sys. Conf., Washington, DC, Feb. 1996, NASA TM 107101.

149.T.C.L. Sollner, W.G. Lyons, D.R. Arsenault, A.C. Anderson, M.M. Seavor, R.B. Boisvert, and R.L. Slattery, Superconducting Cueing Receiver for Space Experiment, IEEE Trans. Applied Superconductivity, Vol 5, No. 2, pp 2071-2074, 1995.

150.H.H.S. Javadi, J.G. Bowen, D.L. Rascoe, R.R. Romanofsky, C.M. Chorey, and K.B. Bhasin, Jet Propulsion Laboratory/NASA Lewis Research Center Space Qualified Hybrid High Temperature Superconducting/Semiconducting 7.4 GHz Low-Noise Downconverter for NRL-NTSSE-II Program IEEE Trans. MTT, Vol.44, No. 7, pp. 1279-1288, 1996.

151.S.M.Sze, Physics of Semiconductors, John Wiley & Sons, 1981.